Materials Research. 2015; 18(6): 1313-1321
DOI: http://dx.doi.org/10.1590/1516-1439.025215

Iron Doped-$ZrSiO_4$: Structural, Microstructural and Vibrational Characterization

Guillermo Manuel Herrera-Pérez*[a,b]

[a]*Consejo Nacional de Ciencia y Tecnología – CONACYT, Centro de Investigación en Materiales Avanzados – CIMAV, Miguel de Cervantes 120, Chihuahua 31109, Chihuahua, Mexico*
[b]*Departamento de Química Inorgánica, Universitat de Valencia, 46100 Burjassot, Valencia, España*

Received: August 13, 2015; Revised: October 1, 2015

Fe_x-$ZrSiO_4$ is known for the applications in the ceramic industry such as ceramic pigment. In this article, we focus our attention to the structural, microstructural and vibrational changes of Fe_x-$ZrSiO_4$ from free-mineralizer precursors, treated at different temperatures in the range of 1100-1600 °C. The refinements of X-ray diffraction patterns show that Fe^{3+} cations were distributed into tetrahedral sites replacing Si^{4+}. The evolution of the shape distribution analyzed by transmission electron microscopy, reveal a polyhedral morphology at 1100 °C during 3h. In comparison, well-rounded and homogeneous particle size was determined in the sample heated at 1600 °C during 24 h. On the other hand, it was observed that increase the content of iron and the increased heat treatment (temperature and time) both plays an important effect on the observed Raman results. The profile line deconvolution applied through the ν_3 vibration of the SiO_4 group shows a spectral change similar to that seen in radiation-damaged zircon: a decrease in frequency and increase in bandwidth.

Keywords: *ceramic pigments, zircon, Rietveld, Raman*

1. Introduction

Electronic and vibrational properties of nanometric doped zirconium silicate ($ZrSiO_4$) are of considerable interest because of the large number of applications of this compound. $ZrSiO_4$, commonly called zircon is widely used in the ceramic, foundry and refractory industries, Zircon adopts a garnet-related structure (Figure 1) having lattice parameters a = 6.607(1) Å; c = 5.982(1) Å, Z = 4[1-3]. The zircon structure can be described as built of chains of alternating edge-sharing SiO_4 tetrahedra and ZrO_8 triangular dodecahedra extending parallel to the c-axis, which are joined laterally by edge-sharing dodecahedra[4-6]. This oxide exhibits low thermal expansion[7], low thermal conductivity, and high resistance to thermal shock[7], as well as good corrosion resistance (for example, against glass melts, slag and liquid metal alloys). Furthermore, a large variety of transition and/or rare-earth metal cations can be incorporated into the host lattice. It is for this reason that zircon is often considered as a natural host material for the storage of radioactive waste material[8-11]. $ZrSiO_4$ is also considered as a promising alternative to silicon oxide as the gate dielectric material in metal-oxide semiconductor devices because of its high permittivity[12].

For Fe doped-$ZrSiO_4$ compound, it is vital interest to gain a fundamental understanding of the influence of size and shape morphology; aggregation of several particles leading to defects in the structure of particles and improvement of crystallinity, which mediate the oxygen ion transport, on the functional properties. In the last decade, several authors have studied different topics referred to the structural and chemical characteristics of Fe-$ZrSiO_4$ [10-24]. The mechanism of formation, the chemical state, and location of Fe cation in the zircon structure, the actual presence of segregated hematite and dissociation of zircon[25-27] have been considered as main topics. In this context, our work over the last few years has been to develop Fe-containing zircon solid solution materials from free-mineralizer precursors with new potential applications, as for instance in electrocatalytic processes[28,29].

Nasdala et al.[30-33] have introduced Raman spectroscopy as a method to estimate quantitatively the degree of radiation damage in zircon. In particular, the peak profile of Raman ν_3 (SiO_4) band at approximately 1,000 cm^{-1} has been used to predict the thermal history of zircon, and this one quantifies the degree of short order around the fourfold Si sites. Nasdala et al.[34] used the width to estimate the possible thermal history of natural zircons, whereas Geisler et al.[35] proposed the use of both the width and frequency to trace potential thermal alterations. They showed that Raman spectra clearly shift towards lower wavenumbers and broaden, which reflects the loss of short-range order and the general expansion of the lattice. The FWHM (full width at half maximum) of the internal ν_3 mode was found to increase most sensitively with increasing radiation damage. It increases from 2 cm^{-1} for well-crystallized (i.e., undamaged) to well above 30 cm^{-1} for strongly radiation-damaged zircon.

Based on these facts, the motivation of the present work is to investigate and demonstrate that the increase of Fe content in $ZrSiO_4$ prepared by the sol-gel technique plays an important role over size effects during the heat treatments and it has an important influence on the intensity, shift symmetry and bandwidth of the Raman results. The first goal was to prepare a series of Fe_x–$ZrSiO_4$ solid solutions from free-mineralizer precursors with increasing content of Fe. The gels were annealed at 1100 °C during 3h, 1200 °C

*e-mail: guillermo.herrera@cimav.edu.mx, guillermo.m.herrera@uv.es

during 3 h and 1600 °C during 24 h. The last temperature and holding time was selected to improve the densification of the material. Our second purpose was to estimate the solubility limit of iron in the zircon structure (in particular in the sample heated at 1600 °C) and compare and elucidate the crystal parameters of the samples by the X-ray diffraction (XRD) Rietveld refinements. The particle size evolution was monitored by transmission electron microscopy (TEM) as the Fe concentration increased. In the third goal, the Raman investigations are motivated by the close relation between the asymmetric broadening of Raman peaks with the crystal-chemical effects such as the tetrahedral distortion determined by the XRD Rietveld refinements.

2. Experimental Procedure

2.1. Samples preparation

Gels with stoichiometry, Fe_X–$ZrSiO_4$, where $x = 0$, 0.02, 0.05, 0.07, 0.1 and 0.125 were prepared by the sol–gel liquid phase route, using zirconium n-propoxide (ZnP, $Zr(OC_3H_7)_4$) tetraethylorthosilicate (TEOS, $Si(OC_2H_5)_4$) and iron acetylacetonate ($Fe(AcAc)_3$, $FeC_{15}H_{24}O_6$), as sources for Zr, Si and Fe, respectively. Details of synthesis and structure analysis can be found elsewhere[36,37].

2.2. Characterization techniques

X-ray powder diffraction analysis (Model AXS D5005 Bruker) was performed using a graphite monochromatic CuKα radiation. The diffractograms were run with a step size of 0.02° 2θ and a counting time of 10 sec. Lattice constants and other structural parameters of zircon phase were determined by refinement with the Rietveld technique using Fullprof98[38] available in the software package Winplotr[39]. The Rietveld refinement involved the following parameters: scale factor; zero displacement correction; unit cell parameters; peak profile parameters using a pseudo-Voigt function; and overall temperature factor. The starting structural parameters and atomic positions of tetragonal zirconia[40], monoclinic zirconia[41], hematite[42] and of zircon-type crystal structure[7-9], were taken from the literature. They were also refined and plotted with Diamond 3.21[43] as shown in Figure 1. The morphology of iron-containing zirconia and zircon particles was also examined using transmission electron microscopy (Model 1010, Jeol Ltd., Tokyo, Japan) at an accelerating voltage of 100 kV. Samples were crushed and dispersed in absolute ethyl alcohol and drops of the dispersion were transferred to a specimen copper grid carrying a lacey carbon film. Particle size analyses were carried out by using the Image J software[44]. The Raman spectra were recorder with spectral windows of 3500-100 cm^{-1} in a high performance dispersive Raman Jasco NRS-3100 spectrometer. A L1200/B500 nm grating dispersed the radiation onto a TE-cooled CCD detector. The spectra were excited with a 632.8 nm radiation from a He-Ne ion laser. The laser beam was focused on the sample with an acquisition time of 10 sec. Profile line deconvolution was performed following the approach as described by Presser & Glotzbach[45]. For the undoped sample we determined the true Raman bandwidth to be 3.3 ± 0.1 cm^{-1}. This value falls within the range of the reported values by Presser & Glotzbach[45] and Gucsik et al.[46].

3. Results and Discussion

3.1. X-ray powder diffraction and the Rietveld refinement

The first step of this study was to characterize the thermal stability of Fe_x-$ZrSiO_4$ reactions up to 1600 °C. Figure 2 shows the evolution of X-ray diffraction results for the powders of $Fe_{0.1}$-$ZrSiO_4$ heated at different temperatures. In panel (a) one can observe an important contribution of tetragonal zirconia (t-ZrO_2), hematite and zircon phases on the sample heated at

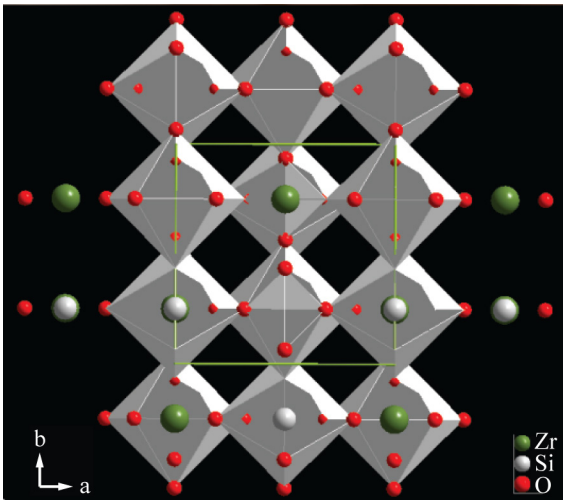

Figure 1. A schematic representation of garnet-type crystal structure of $ZrSiO_4$. The chains of alternating edge-sharing SiO_4 tetrahedra and ZrO_8 dodecahedra projected on (001) and showing the edge sharing between dodecahedra. This representation was obtained by CIF file of Fullprof and it was plotted by Diamond 3.21 software.

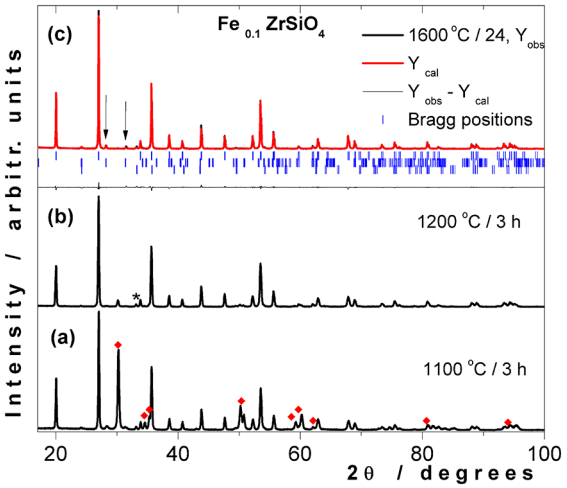

Figure 2. (a) X-ray powder diffraction data for the sample with $Fe_{0.1}$-$ZrSiO_4$ heated at 1100 °C during 3 h (♦ is tetragonal ZrO_2). (b) XRD data for the same composition heated at 1200 °C during 3 h (⁎ is hematite). (c) Rietveld refined X-ray diffraction pattern for the sample with $Fe_{0.1}$-$ZrSiO_4$ powders obtained after the heat treatments at 1600 °C during 24 h. This figure shows the observed intensity (Yobs), the calculated intensity (Ycalc) and the difference between observed and calculated intensities (Yobs - Ycalc) and the vertical lines represents the Bragg positions, (↓ is monoclinic ZrO_2).

1100 °C during 3 h. The XRD pattern obtained at 1200 °C during 3 h shows the decrease in the intensity of the reflections attributed to the t-ZrO_2; the hematite phase still remains and it is indicated by an asterisk in panel (b). Panel (c) shows the XRD for the sample obtained at 1600 °C during 24 h. In this XRD pattern, one can observe the Rietveld refinement profile, the residual profile and the vertical lines (Bragg positions) related to zircon. According to Alahakoon et al.[26], the presence of monoclinic zirconia (m-ZrO_2) indicates that zircon is slightly dissociated at this time and temperature[25]. At this stage, the reflection due to t-ZrO_2 disappearing, confirms the theory that zircon is formed from amorphous silica and m-ZrO_2[26]. Furthermore, at this stage, relatively sharp reflections of hematite crystal phase are resolved in XRD. The detailed structural parameters and goodness of fit between the observed and calculated profiles at selected temperatures are given in Table 1. One can observe from the Rietveld refinement results that a small portion of Fe crystallizes as hematite.

As suggested by Ocaña et al.[47,48] iron must play some role as catalyzer in the zircon formation. Thus, the complete formation of zircon takes place over the range of temperatures between around 1100 °C and 1600 °C depending on the nominal amount of iron. The Rietveld refinements of XRD patterns allowed us to monitor the local distortions of the oxygen around the cations. Table 2 summarized the selected interatomic distances for the samples obtain at 1600 °C during 24 h. In order to perform the calculation we used the structural parameters obtained from Rietveld refinements of the XRD data (CIF file) using Bond Str subprogram in Fullprof[49]. One can observe in Table 2 that the selected interatomic distances reveal a gradual increase in the SiO_4 tetrahedra with increasing iron content up to the sample with 0.07 mol of iron per mol of zircon. On the other hand, one can observe an apparent anomalous variation of the O-O distances.

Figure 3 shows the evolution of the lattice volume against the Fe nominal content in Fe_x–$ZrSiO_4$ solid solutions heated at 1600 °C during 24 h. This behavior is similar to the one reported previously for the samples heated at 1100 °C or 1200 °C[36]. From these results, it can be inferred that the

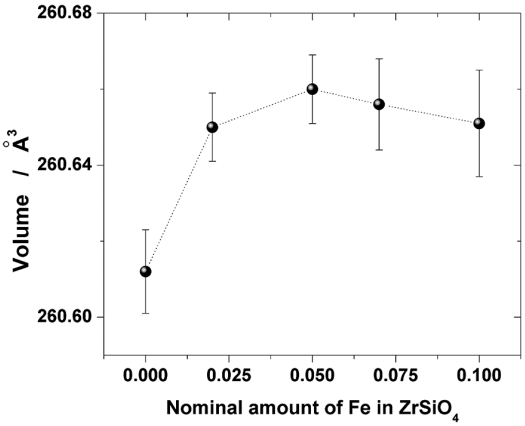

Figure 3. Evolution of lattice volume of Fe_x–$ZrSiO_4$ solid solutions heated at 1600 °C during 24 h as a function of the nominal content of Fe (x).

Table 1. Crystallographic data and results of Rietveld refinement of X-ray diffraction patterns for $Fe_{0.1}$-$ZrSiO_4$ heated at different temperatures.

	1100 °C / 3h	1200 °C / 3h	1600 °C / 24h
a(Å)	6.5993(2)	6.6003(5)	6.6030(7)
c(Å)	5.9777(1)	5.9773(3)	5.9793(4)
V(Å^3)	260.335(4)	260.400(1)	260.702(5)
R_p(%)	8.8	8.6	9.2
R_{wp}(%)	11.6	10.7	12.1
R_{wp} (expected)(%)	7.9	8.1	7.5
χ^2	1.5	1.7	1.6
tetragonal phase (wt %)	30.5	3.4	----
monoclinic phase (wt %)	2.5	1.9	3.5
zircon phase (wt %)	65.5	92.8	93.8
hematite phase (wt %)	1.4	1.9	2.7
Y atomic coordinate of O	0.6649(8)	0.6634(2)	0.6634(2)
z atomic coordinate of O	0.1964(9)	0.1982(3)	0.1993(6)

Table 2. Selected interatomic distances (A) for Fe_x-$ZrSiO_4$ powders heated at 1600 °C during 24 h.

Bond type / Fe_x	0	0.02	0.05	0.07	0.1
Zr - Si					
[2]*	2.9912	2.9895	2.9896	2.9895	2.9897
Zr - O					
[4]	2.1311	2.1117	2.1110	2.1053	2.1147
[4]	2.2681	2.2930	2.2860	2.2880	2.2957
Si – O					
[4]	1.6221	1.6263	1.6318	1.6356	1.6222
O – O					
[1]	2.4302	2.4708	2.4707	2.4799	2.4669
[1]	2.4942	2.5103	2.4945	2.4903	2.5197
[2]	2.7522	2.7435	2.7565	2.7615	2.7355
[4]	2.8422	2.8335	2.8335	2.8321	2.8343
[2]	3.0711	3.0497	3.0499	3.0383	3.0550

*Bracketed numbers are bond multiplicities.

solubility limit is higher than 0.07 mol of iron per mol of zircon (~3.0 wt. % as Fe_2O_3). However, it must be lower than 0.1 mol of Fe (~4.2 wt. % as Fe_2O_3) because in the sample $Fe_{0.1}$–$ZrSiO_4$, hematite is detected as a secondary phase and also a small decrease in its lattice volume. The change of lattice parameters, as the iron content increases in the solid solution, is consistent with the idea of expansion of the lattice, as a larger ion substitutes a small ion. The observed increase in lattice parameters can be understood by assuming that Fe^{3+} replaces Si^{4+} in tetrahedral sites. The larger ionic radius of Fe^{3+} compared with Si^{4+} causes the progressive increase of the unit cell parameters with increasing substitution[36,50]. However, it is to be noted that for reaching electroneutrality in the formation of the Fe-doped zircon solid solution, some oxygen vacancies should be produced. Thus, the probable mechanism could be written out as $Si^{4+} \rightarrow Fe^{3+} + ½O^{2-}$. Furthermore, the simultaneous creation of anion vacancies would be in agreement with the small increase of lattice volume in the Fe-doped zircon series of samples. An alternative simple mechanism of solid solution formation involving the substitution of Zr^{4+} by Fe^{3+} does not seem to be operative because the difference of ionic radius of Zr^{+4} and Fe^{3+} and the simultaneous oxide vacancies creation would give rise to a large decrease in doped-zircon lattice parameters. Carreto et al.[51] studied the preparation of Fe–zircon pigments by the ceramic method adding LiF as mineralizer and reported results on the Fe–zircon solid solution formation[51,52]. They found that only a small fraction of iron, about 2.5 mol %, was hosted in the zircon structure. Strikingly, the trend in the lattice volume variation of Fe–$ZrSiO_4$ solid solutions with increasing the Fe nominal content found by those authors is opposite to the one reported in this work, that is, the lattice volume exhibits a contraction on incorporating the Fe into the zircon lattice. These changes in lattice parameters for samples heated at 1600 °C could be caused by the dissociation of zircon[25,26]. This dissociation will be subjected for a further characterization work.

3.2. Transmission electron microscopy

As a second step, transmission electron micrographs of $Fe_{0.1}$-$ZrSiO_4$ powders without any etching to remove the amorphous silica were collected. Three representative micrographs are show in Figure 4a-c. In Figure 4a it can be observed that the powders heated at 1100 °C during 3 h, the non-aggregated particles shows a small quasi-spherical particles and polyhedral-shape particles. The particle size distribution was determined over the analysis (histograms)

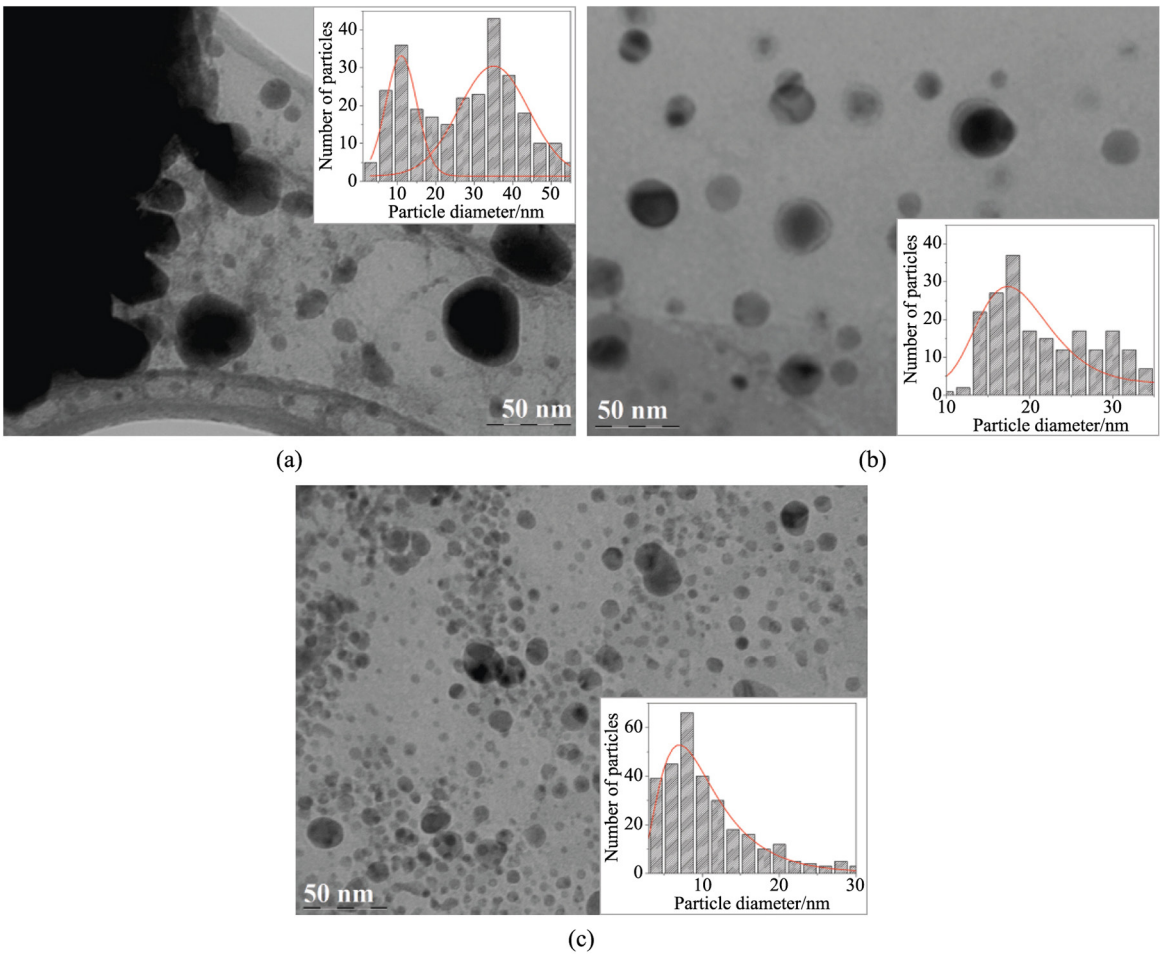

Figure 4. TEM micrographs evolution of $Fe_{0.1}$–$ZrSiO_4$ powders obtained at different temperatures and their respective particle size histogram: (a) Powders heated at 1100 °C during 3 h. (b) Powders heated at 1200 °C during 3 h. (c) Powders heated at 1600 °C during 24 h.

of five micrographs. The results show a bimodal particle size distribution center at 11 ± 2 nm and 35 ± 2 nm, respectively. TEM micrograph of $Fe_{0.1}$–$ZrSiO_4$ powders heated at 1200 °C during 3 h is display in Figure 4b. As can be seen an arrangement of quasi-spherical particles with the average size around 19 ± 2 nm is observed. At this stage, it seems that the amount of dopant plays an important role in the particle size and shape distribution. We also may assume that almost all previous non-crystalline parts of the sample are recrystallizing at this stage, in favor of the remnant ZrO_2. Figure 4c shows the TEM micrograph for the powders heated at 1600 °C during 24 h. The increase of the heat treatment gives rise to a decrease of zircon particle size. The results shows well-rounded particles exhibiting a particle size distribution center at 29 ± 1 nm.

3.3. Raman spectroscopy

The next objective was to characterize the Raman evolution for Fe_x-$ZrSiO_4$ powders in order to monitor the structural changes. Figure 5 shows the evolution of the Raman spectra obtained for $Fe_{0.1}$–$ZrSiO_4$ powders heated at different temperatures. Panel (a) of Figure 5 shows the Raman spectrum after a heat treatment at 1100 °C during 3 h, this result supports the interpretation of XRD showed in Figure 3a. The space group for zircon ($ZrSiO_4$) is $I4_1/amd$, Z=4, D^{19}_{4h}, No. 141[53] and from group theory considerations, 12 Raman active modes are predicted ($2A_{1g} + 4B_{1g} + B_{2g} + 5E_g$)[54-61]. According to Nicola & Rutt[54] and Dawson et al.[55], the most intensive Raman bands of zircon, which lie in the wavenumber range 350-450 cm^{-1} and around 1000 cm^{-1}, must be interpreted as internal vibrations of the SiO_4 units. Intense external lattice vibrations (rotational and translational) occur in the range 200-230 cm^{-1}. On the other hand, zirconium oxide (ZrO_2) exists in three polymorphic forms, namely: (1) monoclinic, which has space group $P2_1/b$ (C^5_{2h}) and Z = 4. It has 18 Raman active modes $9A_g + 9B_g$; (2) the tetragonal phase (ZrO_2), space group $P4_2/mnc$ (D^{15}_{4h}) and Z = 2. It has six Raman active modes, $A_{1g} + 2B_{1g} + 3E_g$; and (3) the cubic phase, space group Fm3m (O^5_h), Z = 4 with only one Raman active mode[56]. Hematite belongs to the D^6_{3d} crystal space group and seven phonon lines are expected in the Raman spectrum[55,56], namely two A_{1g} modes (225 and 498 cm^{-1}) and five E_g modes (247, 293, 299, 412 and 613 cm^{-1}). The positions of the characteristic Raman bands of this work are generally in good agreement with those reported in the literature[57-63]. One can observe that the frequency of the $\nu_3(SiO_4)$ band shows a shift by about 2 cm^{-1} toward lower wavenumbers, when compared with undoped crystalline zircon (Table 3).

Analogously, the Raman spectrum at 1200 °C (Figure 5b) show the bands of zircon, t-ZrO_2 and hematite as one can observe in the XRD pattern (Figure 3b). At this stage $\nu_3(SiO_4)$ FWHM shows a notable broadening by about 10.3 cm^{-1} and a clear shift approximately of 4 cm^{-1} from undoped $ZrSiO_4$. In panel (c) of Figure 6 shows the Raman spectrum for the sample heated at 1600 °C during 24 h, this one confirms the presence of zircon, m-ZrO_2 and hematite. This spectrum shows the gradual increase back to the initial value of 1008 cm^{-1}, however it shows an increase in the FWHM around 15.2 cm^{-1}. Considering these observations and the fact that Fe and heat treatments causes changes in the crystal size and structure; in the next part of this study we focus on the most intensive Raman bands of zircon (between 960-1020 cm^{-1}) in order to discuss the effects of Fe, in particular on the samples obtained at 1600 °C during 24 h. It can be observe from Figure 6 that the Raman peak position shows a systematic red shift on going from the undoped sample to the sample with x=0.05. On the other hand, as one increase the iron concentration from x=0.05 to x=0.1, a reverse trend in the peak position is observed, i.e. a systematic blue shift of the peak position. According to Nasdala et al.[64] the slight shift toward higher vibrational energies is due to the compressive strain in small $ZrSiO_4$ particles, which increases with decreasing particle size. Figure 6 also shows the deconvoluted spectra of $\nu_3(SiO_4)$ and $\nu_1(SiO_4)$ modes for the samples heated at 1600 °C during 24 h. All spectra were fitted with a Gaussian-Lorentzian

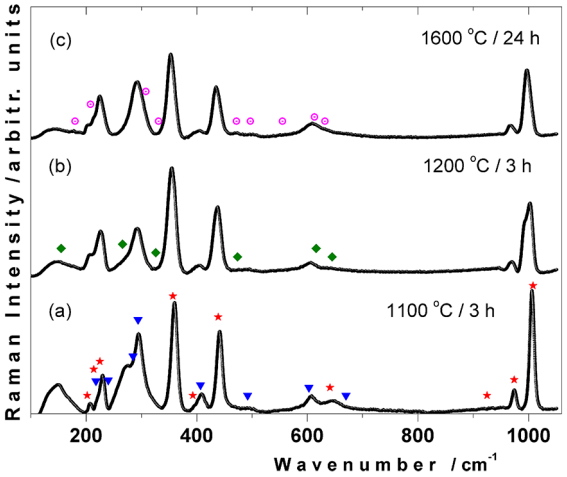

Figure 5. Room temperature Raman spectra for $Fe_{0.1}$-$ZrSiO_4$ powders (a) heated at 1100 °C during 3 h (b) heated at 1200 °C during 3 h and (c) heated at 1600 °C during 24 h. (* is zircon; ▼is hematite, ○ is monoclinic ZrO_2 and ♦ is tetragonal ZrO_2).

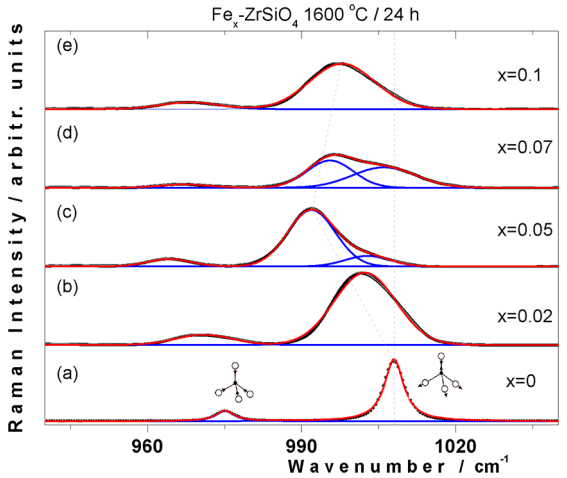

Figure 6. (a-e) Raman spectra evolution for powders of Fe_x-$ZrSiO_4$ to demonstrate band deconvolution obtained at symmetric stretching (ν_1; A_{1g} mode at 974 cm^{-1}) and antisymmetric stretching (ν_3; B_{1g} mode at 1008 cm^{-1}) of SiO_4 tetrahedra. Individual's peaks were fitted by Gauss-Lorentz functions.

Table 3. Results obtained from the profile* deconvolution of selected Raman peak positions and corrected bandwidth values (full width at half maximum, FWHM) for Fe_x-$ZrSiO_4$ powders heated at 1600 °C during 24 h.

Fe_x	0.00		0.02		0.05		0.07		0.1	
Modes	**Peak position (cm^{-1})**	**FWHM (cm^{-1})**	**Peak position (cm^{-1})**	**FWHM (cm^{-1})**	**Peak position (cm^{-1})**	**FWHM (cm^{-1})**	**Peak position (cm^{-1})**	**FWHM (cm^{-1})**	**Peak position (cm^{-1})**	**FWHM (cm^{-1})**
B_{1g} $\nu_3(SiO_4)$	1007.9	3.3	1002.3	10.9	991.9	8.2	995.5	7.9	997.6	11.7
A_{1g} ν_1 (SiO_4)	975.1	3.1	970.9	9.9	964.2	7.5	967.2	7.5	968.1	10.2
A_{1g} ν_2 (SiO_4)	438.7	6.8	438.3	14.0	432.9	14.7	435.8	15.9	435.8	12.8
E_g	357.2	5.5	355.8	14.7	350.9	13.3	354.5	17.8	353.5	12.9

*Averaged at least over five analysis.

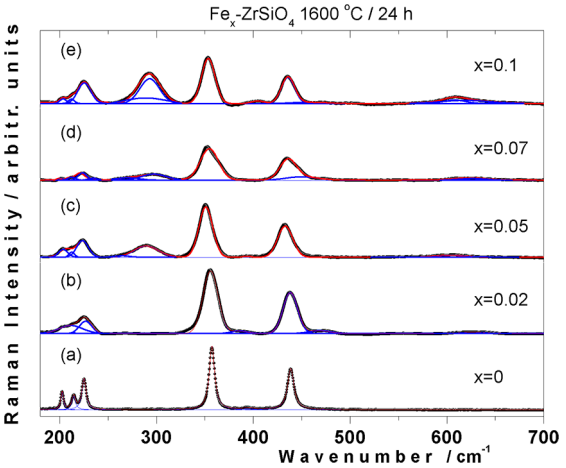

Figure 7. (a-e) Raman spectra evolution and the result of fitting Gauss-Lorentz functions for Fe_x-$ZrSiO_4$ powders in the region between 180-700 cm^{-1}.

type profile to estimate their peak position and its full width half maximum (FWHM). The estimated values of the peak positions and FWHMs are list in Table 3. It can be observe from this table that the peak position of the $\nu_3(SiO_4)$ Raman mode has the lowest value of 1007.9 cm^{-1} at undoped sample and this value gradually shifted to lower wavenumbers with respect to this one. In addition, one can observe a pronounce asymmetry as one increases the iron content. Now we will discuss the mechanism of the wavenumber shift of the $\nu_3(SiO_4)$ mode. Several factors such as temperature, defects and stress can cause a significant shift in the Raman peak position. According to Balkanski et al.[65] and Verma et al.[66] temperature causes shift and broadening of Raman bands. In the present case, all measurements were performed at room temperature. It may be noted that high laser power can cause significant thermal effect, which can result in the broadening and shift of the Raman band[67]. Defects in the structure also cause shifts of the Raman peaks and significant broadening of Raman line shape. The defects in Fe-$ZrSiO_4$ can in fact double the Raman line width. The shift of all main Raman bands (Figure 6, Figure 7 and Table 3) toward lower wavenumbers indicates that in general the average distances between atoms become somewhat larger. As already mentioned in the XRD section concerning the lattice is slightly expanded (Table 2). The increase in band full-width and the accompanying decrease of intensity can be interpreted in such a way that the distribution of bond lengths and bond angles within and between SiO_4 tetrahedra becomes increasingly irregular. The discrepancy between the Raman and XRD evaluation of lattice parameters is due to the fact the XRD is a predominantly probe of long order and Raman is a probe of short order. Also mathematical formalism behind each method that investigates the line broadening is different, resulting in different results.

4. Conclusions

Structural, microstructural and vibrational properties of Fe_x-$ZrSiO_4$ from free-mineralizer precursors were investigated as a function of heat treatments. XRD, TEM and Raman analyses demonstrated that iron plays an important role over the crystal size and shape distribution in Fe-$ZrSiO_4$. The increase in lattice parameters determined by the Rietveld refinement of XRD patterns is consistent with the idea that Fe^{3+} cations are distributed mainly into tetrahedral sites replacing Si^{4+}. The solubility limits of Fe3+ in ZrSiO4 at 1600 °C are in the range 0.07-0.1 mol of iron per mol of zircon. The evolution of particle size and shape distribution reveals a polyhedral morphology at 1100 °C during 3 h. The well-rounded and homogeneous particle size and shape distribution was determined in the sample heated at 1600 °C during 24 h. The Raman spectra for Fe_x-$ZrSiO_4$ treated at different temperatures in the range 1100-1600 °C shows that, as the iron content increases, all Raman bands decrease in intensity becoming increasingly broader and show a notable shift toward lower wavenumbers. These changes suggest that the bond length of SiO_4 tetrahedra become increasingly irregular and the lattice is slightly expanded.

Acknowledgements

G. Herrera thanks Mexico-CONACyT for the student fellowship Grant No. 170588; Postdoctoral Research Scholarship No. 129569 and No. 172529. GH is also indebted with A. Moreno for the library facilities at PUEC-UNAM (Mexico) and L. R. Jiménez-Velasquez and G. Rojas-George. The author also thanks to M.Sc. A. Mestre (SCSIE-Universitat de Valencia) for their assistance in XRD measurements and M.Sc. M. Alcalde for Raman measurements performed at Universitat Jaume I.

References

1. Berry FJ, Eadon D, Holloway J and Smart LE. Iron doped zirconium silicate. Part 1: the location of iron. *Journal of Materials Chemistry*. 1996; 6(2):221-225. http://dx.doi.org/10.1039/jm9960600221.
2. Tartaj P, González-Carreño T, Serna CJ and Ocaña M. Iron zircon pigments prepared by pyrolysis of aerosols. *Journal of Solid State Chemistry*. 1997; 128(1):102-108. http://dx.doi.org/10.1006/jssc.1996.7176.
3. Bondioli F, Ferrari AM, Leonelli C and Manfredini T. Syntheses of Fe_2O_3/silica red inorganic inclusion pigments for ceramic applications. *Materials Research Bulletin*. 1998; 33(5):723-729. http://dx.doi.org/10.1016/S0025-5408(98)00047-6.
4. Robinson K, Gibbs GV and Ribbe PH. The structure of zircon: a comparison with garnet. *American Mineralogist.* 1971; 56:782-790.
5. Hazen RM and Finger LW. Crystal structure and compressibility of zircon at high pressure. *American Mineralogist.* 1979; 64:196-201.
6. Finch JR and Hanchar JM. Structure and chemistry of zircon and zircon-group minerals. *Reviews in Mineralogy and Geochemistry*. 2003; 53(1):1-25. http://dx.doi.org/10.2113/0530001.
7. Mori T, Yamamura H, Kobayashi H and Mitamura T. Preparation of high-purity $ZrSiO_4$ powder using sol-gel processing and mechanical properties of the sintered body. *Journal of the American Ceramic Society*. 1992; 75(9):2420-2426. http://dx.doi.org/10.1111/j.1151-2916.1992.tb05594.x.
8. Ewing RC and Lutze W. Disposing of plutonium. *Science*. 1997; 275(5301):737-741. http://dx.doi.org/10.1126/science.275.5301.737a.
9. Ewing RC. Nuclear waste forms for actinides. *Proceedings of the National Academy of Sciences of the United States of America*. 1999; 96(7):3432-3439. http://dx.doi.org/10.1073/pnas.96.7.3432. PMid:10097054.
10. Burakov BE, Hanchar JM, Zamoryanskaya MV, Garbuzov VM and Zirlin VA. Synthesis and investigation of Pu-doped single crystal zircon, $(Zr, Pu)SiO_4$. *Radiochimica Acta*. 2002; 89:1-3.
11. Ewing RC, Lutze W and Weber W. Zircon: a host-phase for the disposal of weapons plutonium. *Journal of Materials Research*. 1995; 10(02):243-246. http://dx.doi.org/10.1557/JMR.1995.0243.
12. Smirnov MB, Sukhomlinov SV and Smirnov SK. Vibrational spectrum of reidite $ZrSiO_4$ from first principles. *Physical Review B: Condensed Matter and Materials Physics*. 2010; 82(9):0943071. http://dx.doi.org/10.1103/PhysRevB.82.094307.
13. Berry FJ, Eadon D, Holloway J and Smart LE. Iron-doped zircon: the mechanism of formation. *Journal of Materials Science*. 1999; 34(15):3631-3638. http://dx.doi.org/10.1023/A:1004691019526.
14. Llusar M, Badenes JA, Calbo J, Tena MA and Monrós G. Estudio del efecto de la adición de distintos mineralizadores en la síntesis cerámica del pigmento rosa coral de hierro-circón. *Boletín de la Sociedad Española de Cerámica y Vidrio*. 1999; 38:201-208.
15. Shoyama M, Hashimoto K, Hashimoto T, Nasu H and Kamiya K. Iron-zircon pigments prepared by the sol-gel method. *Journal of the Ceramic Society of Japan*. 1999; 107(1246):534-540. http://dx.doi.org/10.2109/jcersj.107.534.
16. Llusar M, Badenes JA, Calbo J, Tena MA and Monrós G. Environmental and colour optimisation of mineraliser addition in synthesis of iron zircon ceramic pigment. *British Ceramic Transactions*. 2000; 99(1):14-22. http://dx.doi.org/10.1179/bct.2000.99.1.14.
17. Llusar M, Calbo J, Badenes JA, Tena MA and Monrós G. Synthesis of iron zircon coral by coprecipitation routes. *Journal of Materials Science*. 2001; 36(1):153-163. http://dx.doi.org/10.1023/A:1004801406230.
18. Ardizzone S, Binaghi L, Cappelletti G, Fermo P and Gilardoni S. Iron doped zirconium silicate prepared by a sol–gel procedure. The effect of the reaction conditions on the structure, morphology and optical properties of the powders. *Physical Chemistry Chemical Physics*. 2002; 4(22):5683-5689. http://dx.doi.org/10.1039/b207381a.
19. García A, Llusar M, Sorlí S, Calbo J, Tena MA and Monrós G. Effect of the surfactant and precipitant on the synthesis of pink coral by a microemulsion method. *Journal of the European Ceramic Society*. 2003; 23(11):1829-1838. http://dx.doi.org/10.1016/S0955-2219(02)00451-X.
20. Cortés EC, Fuente JAM, Moreno JM, Pérez CP, Cordoncillo EC and Castelló JBC. Solid-solution formation in the synthesis of fe-zircon. *Journal of the American Ceramic Society*. 2004; 87(4):612-616. http://dx.doi.org/10.1111/j.1551-2916.2004.00612.x.
21. Cappelletti G, Ardizzone S, Fermo P and Gilardoni S. The influence of iron content on the promotion of the zircon structure and the optical properties of pink coral pigments. *Journal of the European Ceramic Society*. 2005; 25(6):911-917. http://dx.doi.org/10.1016/j.jeurceramsoc.2004.04.023.
22. Ozel E and Turan S. Production of coloured zircon pigments from zircón. *Journal of the European Ceramic Society*. 2007; 27(2-3):1751-1757. http://dx.doi.org/10.1016/j.jeurceramsoc.2006.05.008.
23. Pyon K-R and Lee B-H. Effect of iron content and annealing temperature on the color characteristics of Fe-$ZrSiO_4$ coral pink pigments synthesized by Sol-gel method. *Journal of the Ceramic Society of Japan*. 2009; 117(1363):258-263. http://dx.doi.org/10.2109/jcersj2.117.258.
24. Yu R, Kim YJ, Pee JH, Kim KJ and Kim W. Thermal behavior and coloration study of silica-coated alpha-Fe_2O_3 and beta-FeOOH nanocapsules. *Journal of Nanoscience and Nanotechnology*. 2011; 11(7):6283-6286. http://dx.doi.org/10.1166/jnn.2011.4379. PMid:22121702.
25. Kaiser A, Lobert M and Telle R. Thermal stability of zircon ($ZrSiO_4$). *Journal of the European Ceramic Society*. 2008; 28(11):2199-2211. http://dx.doi.org/10.1016/j.jeurceramsoc.2007.12.040.
26. Alahakoon WPCM, Burrows SE, Howes AP, Karunaratne BSB, Smith ME and Dobedoe RS. Fully densified zircon co-doped with iron and aluminium prepared by sol-gel processing. *Journal of the European Ceramic Society*. 2010; 30(12):2515-2523. http://dx.doi.org/10.1016/j.jeurceramsoc.2010.05.011.
27. Kock LD, Lekgoathi MDS, Snyders E, Wagener JB, Nel JT and Havenga JL. The determination of percentage dissociation of zircon ($ZrSiO_4$) to plasma-dissociated zircon (ZrO_2•SiO_2) by Raman spectroscopy. *Journal of Raman Spectroscopy : JRS*. 2012; 43(6):769-773. http://dx.doi.org/10.1002/jrs.3090.
28. Herrera G, Montoya N, Doménech-Carbó A and Alarcón J. Synthesis, characterization and electrochemical properties of iron-zirconia solid solution nanoparticles prepared using a sol-gel technique. *Physical Chemistry Chemical Physics*. 2013; 15(44):19312-19321. http://dx.doi.org/10.1039/c3cp53216j. PMid:24121534.
29. Doménech-Carbó A, Herrera G, Montoya N, Pardo P, Alarcón J, Doménech-Carbó T, et al. Solid state electrochemistry of iron-doped zircon and zirconia materials. *Journal of the Electrochemical Society*. 2014; 161:H539-H546. http://dx.doi.org/10.1149/2.0751409jes.
30. Nasdala L, Irmer G and Wolf D. The degree of metamictization in zircon a Raman spectroscopic study. *European Journal of*

Mineralogy. 1995; 7(3):471-478. http://dx.doi.org/10.1127/ejm/7/3/0471.

31. Nasdala L, Irmer G and Jonckheere R. Metamictisation of natural zircon: accumulation versus thermal annealing of radioactivity-induced damage. *Contributions to Mineralogy and Petrology*. 2002; 143(6):758-765. http://dx.doi.org/10.1007/10.1007/s00410-002-0380-7.
32. Nasdala L, Zhang M, Kempe U, Panczer G, Gaft M, Andrut M, et al. Spectroscopic methods applied to zircon. *Reviews in Mineralogy and Geochemistry*. 2003; 53(1):427-467. http://dx.doi.org/10.2113/0530427.
33. Nasdala L, Miletich R, Ruschel K and Váczi T. Raman study of radiation-damaged zircon under hydrostatic compression. *Physics and Chemistry of Minerals*. 2008; 35(10):597-602. http://dx.doi.org/10.1007/s00269-008-0251-5.
34. Nasdala L, Wenzel M, Vavra G, Irmer G, Wenzel T and Kober B. Metamictisation of natural zircon: accumulation versus thermal annealing of radioactivity-induced damage. *Contributions to Mineralogy and Petrology*. 2001; 141(2):125-144. http://dx.doi.org/10.1007/s004100000235.
35. Geisler T, Pidgeon RT, van Bronswijk W and Pleysier R. Kinetics of thermal recovery and recrystallization of partially metamict zircon: a Raman spectroscopic study. *European Journal of Mineralogy*. 2001; 13(6):1163-1176. http://dx.doi.org/10.1127/0935-1221/2001/0013-1163.
36. Herrera G, Montoya N and Alarcón J. Synthesis and characterization of iron-doped $ZrSiO_4$ solid solutions from gels. *Journal of the American Ceramic Society*. 2011; 94(12):4247-4255. http://dx.doi.org/10.1111/j.1551-2916.2011.04808.x.
37. Herrera G, Montoya N and Alarcón J. Microstructure of Fe–$ZrSiO_4$ solid solutions prepared from gels. *Journal of the European Ceramic Society*. 2012; 32(1):227-234. http://dx.doi.org/10.1016/j.jeurceramsoc.2011.08.014.
38. Rodriguez-Carvajal J. FULLPROF: a program for rietveld refinement and pattern matching analysis. In: *Abstracts of the Satellite Meeting on Powder Diffraction of the XV Congress of the International Union of Crystallography*; 1990; Toulouse, France. Toulouse: IUCr; 1990. p. 127.
39. Rodriguez-Carvajal J and Roisnel T. Fullprof.98 and WinPLOTR New Windows 95/NT applications for diffraction. *Newsletter*. 1998; 20:35-36.
40. Teufer G. The crystal structure of tetragonal ZrO_2. *Acta Crystallographica*. 1962; 15(11):1187. http://dx.doi.org/10.1107/S0365110X62003114.
41. Smith DK and Newkirk HW. The crystal structure of baddeleyite (monoelinie ZrOz) and its relation to the polymorphism of ZrO_2. *Acta Crystallographica*. 1965; 18(6):983-991. http://dx.doi.org/10.1107/S0365110X65002402.
42. Blake RL, Hessevick RE, Zoltai T and Finger LW. Refinement of the hematite structure. *American Mineralogist*. 1966; 51:123-129.
43. Bergerhoff G, Berndt M and Brandenburg K. Evaluation of crystallographic data with the program DIAMOND. *Journal of Research of the National Institute of Standards and Technology*. 1996; 101(3):221-225. http://dx.doi.org/10.6028/jres.101.023.
44. Rasband WS. *ImageJ*. Bethesda: U.S. National Institutes of Health. Available from: <http://imagej.nih.gov/ij>. Access in: 13 Aug. 2015.
45. Presser V and Glotzbach C. Metamictization in zircon: Raman investigation following a Rietveld approach. Part II: Sampling depth implication and experimental data. *Journal of Raman Spectroscopy*. 2009; 40(5):499-508. http://dx.doi.org/10.1002/jrs.2154.
46. Gucsik A, Zhang M, Koeberl C, Salje EKH, Redfern SAT and Pruneda JM. Infrared and Raman spectra of $ZrSiO_4$ experimentally shocked at high pressures. *Mining Magazine*. 2004; 68(5):801-811. http://dx.doi.org/10.1180/0026461046850220.
47. Ocaña M, Fórnes V and Serna CJ. The variability of the infrared powder spectrum of amorphous SiO_2. *Journal of Non-Crystalline Solids*. 1989; 107(2-3):187-192. http://dx.doi.org/10.1016/0022-3093(89)90461-4.
48. Ocaña M, Fórnes V and Serna CJ. A simple procedure for the preparation of spherical oxide particles by hydrolysis of aerosols. *Ceramics International*. 1992; 18(2):99-106. http://dx.doi.org/10.1016/0272-8842(92)90038-F.
49. Rodriguez-Carvajal J. Recent advances in magnetic structure determination by neutron powder diffraction. *Physica B, Condensed Matter*. 1993; 192(1-2):55-69. http://dx.doi.org/10.1016/0921-4526(93)90108-I.
50. Shannon RD. Revised effective ionic radii and systematic studies of interatomie distances in halides and chaleogenides. *Acta Crystallographica. Section A, Crystal Physics, Diffraction, Theoretical and General Crystallography*. 1976; 32(5):751-767. http://dx.doi.org/10.1107/S0567739476001551.
51. Carreto E, Piña C, Arriola H, Barahona A C, Nava N and Castaño V. Mössbauer study of the structure of Fe – zircon system. *Journal of Radioanalytical and Nuclear Chemistry*. 2001; 250(3):453-458. http://dx.doi.org/10.1023/A:1017988720055.
52. Cortés EC, Fuente JAM, Moreno JM, Pérez CP, Cordoncillo EC and Castelló JBC. Solid-solution formation in the synthesis of Fe–zircon. *Journal of the American Ceramic Society*. 2004; 87(4):612-616. http://dx.doi.org/10.1111/j.1551-2916.2004.00612.x.
53. Miller SA, Caspers HH and Rast HE. Lattice vibrations of Yttrium Vanadate. *Physical Review*. 1968; 168(3):964-969. http://dx.doi.org/10.1103/PhysRev.168.964.
54. Nicola JH and Rutt HN. A comparative study of zircon ($ZrSiO_4$) and hafnon ($HfSiO_4$) Raman spectra. *Journal of Physics. C. Solid State Physics*. 1974; 7(7):1381-1386. http://dx.doi.org/10.1088/0022-3719/7/7/029.
55. Dawson P, Hargreave MM and Wilkinson GR. The vibrational spectrum of zircon ($ZrSiO_4$). *Journal of Physics. C. Solid State Physics*. 1971; 4(2):240-256. http://dx.doi.org/10.1088/0022-3719/4/2/014.
56. Gazzoli D, Mattei G and Valigi M. Raman and X-ray investigations of the incorporation of Ca^{2+} and Cd^{2+} in the ZrO_2 structure. *Journal of Raman Spectroscopy*. 2007; 38(7):824-831. http://dx.doi.org/10.1002/jrs.1708.
57. Porto SPS and Krishnan RS. Raman effect of corundum. *The Journal of Chemical Physics*. 1967; 47(3):1009-1012. http://dx.doi.org/10.1063/1.1711980.
58. Bhagavantam S and Venkatarayudu T. Raman effect in relation to crystal structure. *Proceedings of the Indian Academy of Sciences - Section A*. 1939; 10:224-258.
59. Faria DLA, Silva SV and Oliveira MT. Raman microspectroscopy of some iron oxides and oxyhydroxides. *Journal of Raman Spectroscopy*. 1997; 28(11):873-878. http://dx.doi.org/10.1002/(SICI)1097-4555(199711)28:11<873::AID-JRS177>3.0.CO;2-B.
60. Jubb AM and Allen HC. Vibrational spectroscopic characterization of hematite, maghemite, and magnetite thin films produced by vapor deposition. *ACS Applied Materials & Interfaces*. 2010; 2(10):2804-2812. http://dx.doi.org/10.1021/am1004943.
61. Kozlova AP, Sugiyama S, Kozlov AI, Asakura K and Iwasawa Y. Iron-oxide supported gold catalysts derived from gold-phosphine complex $Au(PPh_3)(NO_3)$: state and structure of the support. *Journal of Catalysis*. 1998; 176(2):426-438. http://dx.doi.org/10.1006/jcat.1998.2069.

62. Legodi MA and de Waal D. The preparation of magnetite, goethite, hematite and maghemite of pigment quality from mill scale iron waste. *Dyes and Pigments*. 2007; 74(1):161-168. http://dx.doi.org/10.1016/j.dyepig.2006.01.038.

63. Shim S-H and Duffy TS. Raman spectroscopy of Fe_2O_3 to 62 GPa. *The American Mineralogist*. 2001; 87(2-3):318-326. http://dx.doi.org/10.2138/am-2002-2-314.

64. Nasdala L, Lengauer CL, Hanchar JM, Kronz A, Wirth R, Blanc P, et al. Annealing radiation damage and the recovery of cathodoluminescence. *Chemical Geology*. 2002; 191(1-3):121-140. http://dx.doi.org/10.1016/S0009-2541(02)00152-3.

65. Balkanski M, Wallis RF and Haro E. Anharmonic effects in light scattering due to optical phonons in silicon. *Physical Review B: Condensed Matter and Materials Physics*. 1983; 28(4):1928-1934. http://dx.doi.org/10.1103/PhysRevB.28.1928.

66. Verma P, Abbi SC and Jain KP. Raman-scattering probe of anharmonic effects in GaAs. *Physical Review B: Condensed Matter and Materials Physics*. 1995; 51(23):16660-16667. http://dx.doi.org/10.1103/PhysRevB.51.16660. PMid:9978670.

67. Gouadec G and Colomban P. Raman Spectroscopy of nanomaterials: how spectra relate to disorder, particle size and mechanical properties. *Progress in Crystal Growth and Characterization of Materials*. 2007; 53(1):1-56. http://dx.doi.org/10.1016/j.pcrysgrow.2007.01.001.